

# Instability Driven by a Finitely Thick Annular Beam in a Dielectric-Loaded Cylindrical Waveguide

Shusuke TAMURA, Mitsuhsa YAMAKAWA, Yusuke TAKASHIMA and Kazuo OGURA

*Graduate School of Science and Technology, Niigata University, Niigata 950-2181, Japan*

(Received 16 November 2007 / Accepted 11 March 2008)

The Cherenkov and slow cyclotron instabilities driven by an axially injected electron beam in a cylindrical waveguide are studied using a new version of the self-consistent linear theory considering three-dimensional beam perturbations. There are three kinds of models for beam instability analysis, which are based on a cylindrical solid beam, an infinitesimally thin annular beam, and a finitely thick annular beam. Among these models, the beam shape properly representing the often used actual annular electron beams is the finitely thick annulus. We develop a numerical code for a cylindrical waveguide with a finitely thick annular beam. Our theory is valid for any beam velocity. We present eigen-modes of the cylindrical system with the plasma and beam. Instabilities driven by the annular beam in a dielectric-loaded waveguide are also examined.

© 2008 The Japan Society of Plasma Science and Nuclear Fusion Research

Keywords: annular beam, finite thickness, low-frequency surface wave mode, high-frequency surface wave mode, Cherenkov instability, slow cyclotron instability

DOI: 10.1585/pfr.3.S1020

## 1. Introduction

A backward wave oscillator (BWO) or a traveling wave tube (TWT) is one of the high power microwave sources and can be driven by an axially injected electron beam without initial perpendicular velocity. For relatively low powers (tens of kW or less), Pierce type thermionic cathodes are commonly used, and the beam shape is approximated by a cylindrical solid beam [1]. In many high power experiments, cold cathodes are used, and the shape of the electron beam is a thin-walled annulus [2].

For a cylindrical solid beam, a new version of the self-consistent field theory considering three-dimensional beam perturbations was developed in Refs. [3, 4]. For an infinitesimally thin annular beam, the boundary is modulated by the transverse modulation of the annular surface. Analyses of such beams need to be based on a different theory from that for a solid beam. A pioneering work can be seen in Ref. [5] using a non-relativistic linear theory of the interaction of a sheet beam with distributed circuit elements. The effect of the transverse beam perturbation was considered as a change in beam coupling coefficient to the circuit. Recently, instabilities of eigen modes in an infinitesimally thin annular beam were analyzed [6], presenting a new field theory considering the moving surface modulation.

For finitely thick annular beam, the boundary condition at the beam surface is different from that for an infinitesimally thin annular beam. The boundary condition for a finitely thick annular beam is similar to that of a solid beam, but the number of boundaries is different. The former has an outside and an inside surface, and the latter has

only an outside surface. In this work, we develop a numerical code for a cylindrical waveguide with an annular beam having an arbitrary thickness. Our numerical codes are valid for any beam velocity  $v$  less than the light velocity, and can study the eigen-modes of a waveguide with annular plasma ( $v = 0$ ) and beam ( $v > 0$ ), and the instabilities driven by the annular beam.

The organization of this paper is as follows. In Sec. 2, we describe our numerical method dealing with a finitely thick annular beam. In Sec. 3, dispersion characteristics of a finitely thick annular plasma are examined, by comparing them with cylindrical solid plasma characteristics. In Sec. 4, the Cherenkov and slow cyclotron instabilities driven by a finitely thick annular beam in a dielectric-loaded waveguide are examined. A discussion and conclusion of this paper are given in Sec. 5.

## 2. Numerical Method

For slow-wave devices, the periodically corrugated slow-wave structure (SWS) is often used [7, 8]. However, analyses of these devices become very complex. Therefore, we analyzed the basic electromagnetic characteristics of a cylindrical waveguide with a straight wall in Fig. 1. We consider a waveguide with a wall radius  $R_w$ . The waveguide is partially loaded with a dielectric from  $R_d$  to  $R_w$ . The relative permittivity of the dielectric is  $\epsilon_r$ . The beam has an average radius  $R$  and thickness  $\Delta_p$ . For a cylindrical solid beam, the beam outside radius is set to  $R_b$ . The cylindrical coordinate system  $(r, \theta, z)$  is used in this study. A guiding magnetic field  $B_0$  is applied uniformly in the  $z$ -direction. An electron beam is propagating along the guiding magnetic field. The temporal and spa-

author's e-mail: f06e072j@mail.cc.niigata-u.ac.jp

tial phase factor of all perturbed quantities is assumed to be  $\exp[i(k_z z + m\theta - \omega t)]$ . Here,  $m$  is the azimuthal mode number, and  $k_z$  is the axial wave number.

In a system with magnetized plasma or a beam such as the one shown in Fig.2, the boundary condition at the beam-vacuum interface should be considered properly. Electron beam surfaces are modulated as the beam is propagating. For finitely thick annular and solid beams, the transverse modulation appears as the surface electric charge at the fixed boundary as shown in Figs.2 and 3. Considering the surface charge, we obtain four indepen-

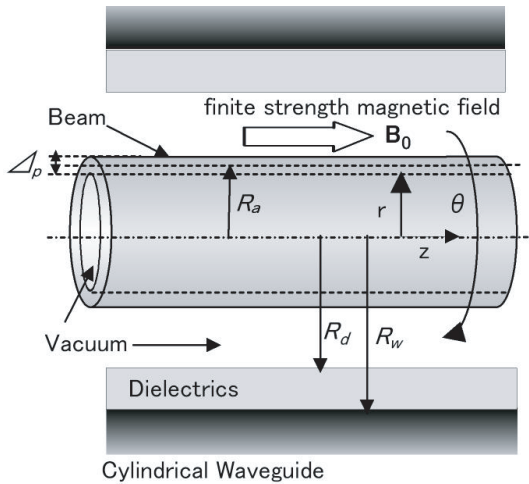


Fig. 1 Model for analysis a thin-walled annular beam.

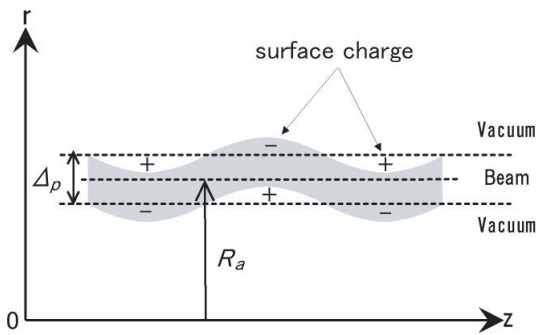


Fig. 2 Beam surface of a thin-walled annular beam.

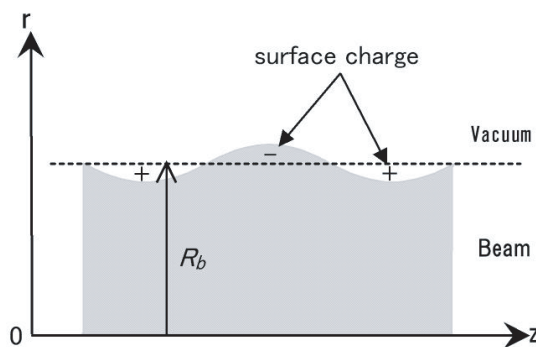


Fig. 3 Beam surface of a solid beam.

dent equations at the beam-vacuum interface. They are for the two tangential components of the electric field, axial component of the magnetic field, and radial component of the electric flux density. At the waveguide wall, the electric field components tangential to the wall should be zero. From these conditions, dispersion relations can be obtained. For the solid beam, the derivation of dispersion relation is provided in Refs. [3, 4]. The solid beam has one surface. The finitely thick annular beam has another surface inside the beam, because there is a vacuum region inside the beam. In Appendix, we summarize the derivation of the dispersion relation using the conditions at both beam boundaries and the waveguide wall.

### 3. Dispersion Curves of Plasma

We present dispersion characteristics of finitely thick annular and solid plasmas, by assuming  $v = 0$ . The waveguide radius is  $R_w = 1.445$  cm, and the inner radius of the dielectric is  $R_d = 0.85$  cm. Plasma and cyclotron frequencies are  $\omega_p$  and  $\Omega$ , respectively. Figures 4-9 show the dispersion curves for the annular plasma with  $R_a = 0.75$  cm and  $\Delta_p = 0.1$  cm, and for the solid plasma with  $R_b = 0.8$  cm. In this section, the plasma angular frequency is  $\omega_p = 3 \times 10^{10}$  rad/s. For the analysis of the plasma, the relative permittivity is set to  $\epsilon_r = 1.0$ , which indicates that there is no dielectric. Figures 4 and 5 show the dispersion curves for the annular and solid plasmas, respectively, in the absence of a magnetic field. Axisymmetric electromagnetic modes are the transverse magnetic  $TM_{0n}$  and transverse electric  $TE_{0n}$  modes. Here,  $n$  is any positive integer.

Dispersion curves of the finitely thick annular plasma show two surface waves due to the inner and outer surface space charges: high- and low-frequency surface wave modes, which are denoted as HSW and LSW, respectively. Solid plasma has only one surface wave mode (SW) due

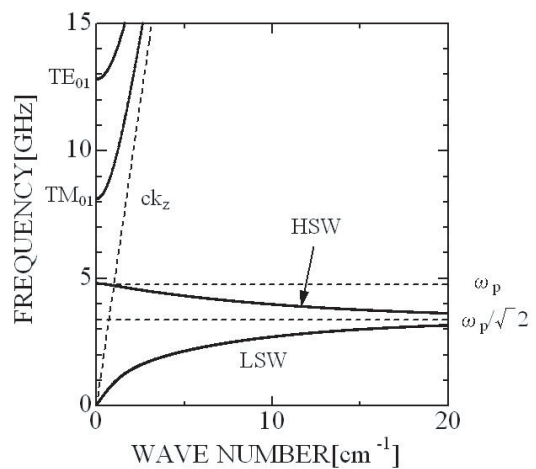


Fig. 4 Dispersion curves of thin-walled annular plasma in the absence of magnetic field.

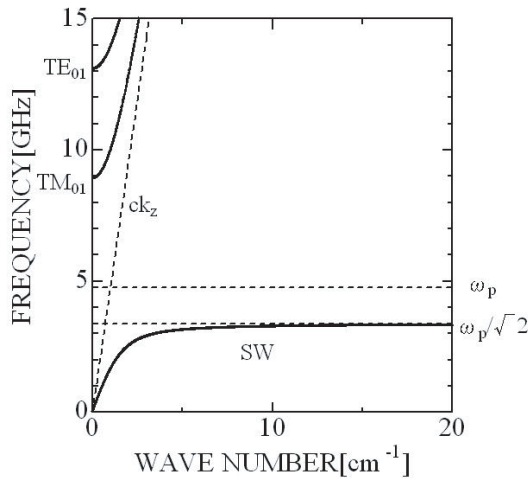


Fig. 5 Dispersion curves of solid plasma in the absence of magnetic field.

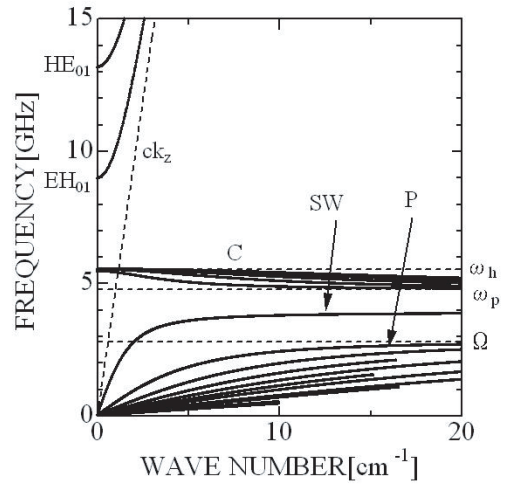


Fig. 7 Dispersion curves of solid plasma with  $B_0 = 0.1$  T.

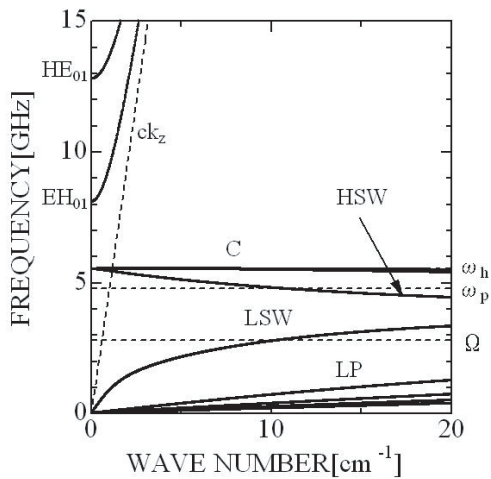


Fig. 6 Dispersion curves of thin-walled annular plasma with  $B_0 = 0.1$  T.

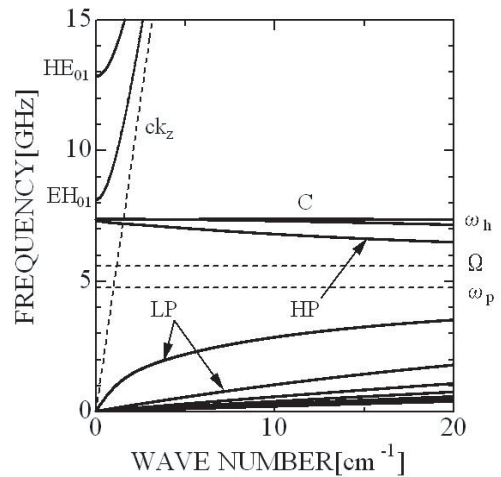


Fig. 8 Dispersion curves of thin-walled annular plasma with  $B_0 = 0.2$  T.

to the outer surface space charge. The LSW is due to the outer surface of the annulus and corresponds to the SW of solid plasma. The frequency is zero at  $k_z = 0$ , increases with increasing  $k_z$ , and approaches an asymptotic limit as  $k_z \rightarrow \infty$ . This limit is  $\omega_p/\sqrt{2}$ . The HSW mode is attributed to the inner boundary of the annular plasma. Its frequency is  $\omega_p$  at  $k_z = 0$ , decreases with increasing  $k_z$ , and approaches an asymptotic limit as  $k_z \rightarrow \infty$ . This limit is also  $\omega_p/\sqrt{2}$ .

The dispersion curves for the annular and solid plasmas are shown in Figs. 6 and 7, respectively, at  $B_0 = 0.1$  T ( $\omega_p > \Omega$ ) and in Figs. 8 and 9, respectively, at  $B_0 = 0.2$  T ( $\Omega > \omega_p$ ). With finite strength magnetic fields, electromagnetic modes become a hybrid of TM and TE modes, even in axisymmetric cases. EH and HE are often used to designate the hybrid mode. In this study, TM is dominant in the EH mode, and TE is dominant in the HE mode. In

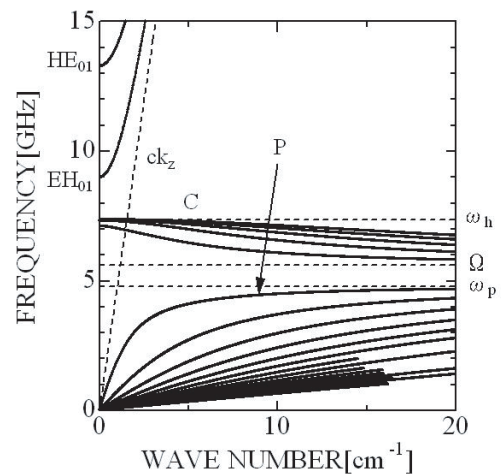


Fig. 9 Dispersion curves of solid plasma with  $B_0 = 0.2$  T.

Figs. 6 and 7, axisymmetric  $\text{EH}_{0n}$  and  $\text{HE}_{0n}$  modes can be seen.

Cyclotron modes, denoted as C in Figs. 6-9, appear in addition to the space charge modes. For both finitely thick annular and solid plasmas, the frequencies of cyclotron mode are between the upper hybrid frequency  $\omega_h = (\Omega^2 + \omega_p^2)^{1/2}$  and  $\Omega$  or  $\omega_p$ , whichever is larger.

As for the space charge modes, surface wave modes like the  $B_0 = 0$  case exist if  $\Omega < \omega_p$ . With increasing  $k_z$ , the frequencies of LSW as well as SW increase from zero and approach an asymptotic limit as  $k_z \rightarrow \infty$ . This limit is not  $\omega_p/\sqrt{2}$  but  $\omega_h/\sqrt{2}$ . The frequency of HSW decreases with increasing  $k_z$ , and has the same asymptotic value as the low-frequency mode in the limit of  $k_z \rightarrow \infty$ .

The presence of a magnetic field lead to the well-known plasma modes due to the volume space charge perturbation [4]; the low-frequency plasma mode (LP) of the annular plasma and plasma mode (P) of the solid plasma in Figs. 6-9. They have frequencies that are zero at  $k_z = 0$ , increase with increasing  $k_z$ , and approach an asymptotic limit as  $k_z \rightarrow \infty$ . This limit is  $\omega_p$  or  $\Omega$ , whichever is smaller.

High-frequency plasma mode (HP) in Fig. 8 is in the frequency range of  $\omega_h > \omega > \Omega$  and approaches  $\Omega$  as  $k_z \rightarrow \infty$ . In terms of the frequency region, it can be said that this mode is a kind of cyclotron mode. However, it is still affected by the inner surface of the annular plasma. When  $\Omega$  is not sufficiently larger than  $\omega_p$  as in Fig. 8, it has qualitatively the same field properties as the high-frequency surface wave mode in Fig. 6 and is pushed down farther than the other cyclotron modes. By increasing the magnetic field further, the inner surface effect becomes negligible.

For the finitely thick annular plasma, the cyclotron modes stay closer to the line  $\omega = \omega_h$ , and plasma modes are pushed down closer to the line  $\omega = 0$  than the solid plasma case. This may be caused by the difference in the geometrical factor. The solid plasma occupies a larger portion of the cylindrical cross section than the annular plasma. At the same  $\omega_p$ , the plasma effects on the eigenmodes of the waveguide are more remarkable for the solid shape than for the annular shape.

For the dielectric-loaded waveguides, eigenmodes are very complicated in themselves. They become more complicated due to the inner boundary of the annulus. We summarize eigenmodes due to the surface and volume space charges in Tables 1 and 2.

For HSW, the signs of surface charges on the inner and outer surfaces are opposite, just as in Fig. 2. The plasma sheet behaves as a electric double layer. On the other hand, the transverse displacements of the inner and outer surfaces are opposite for LSW. The surface charges are of the same sign, and the plasma sheet becomes a charge layer. In the solid plasma case, the surface charge is a charge layer at  $r = R_b$ , as can be seen from Fig. 3.

Cyclotron modes are relatively simple and are denoted as C in Figs. 6-9. When  $\Omega$  is not sufficiently larger than  $\omega_p$ ,

Table 1 Space charge mode of a finitely thick annular plasma.

	$\omega_p > \Omega$	$\Omega > \omega_p$
Surface wave mode due to the outer surface (lower frequency region)	LSW	—
Surface wave mode due to the inner surface (higher frequency region)	HSW	—
Volume space charge mode	LP	

Table 2 Space charge mode of a solid plasma.

	$\omega_p > \Omega$	$\Omega > \omega_p$
Surface wave mode due to the outer surface	SW	—
Volume space charge mode	P	

the lowest branch of C is affected by the inner surface of the annulus, HP in Fig. 8.

## 4. Instabilities Driven by the Finitely Thick Annular Beam

In this section, we examine instabilities driven by beam ( $v > 0$ ). The waveguide radius is  $R_w = 1.445$  cm, and the inner radius of dielectric is  $R_d = 0.85$  cm. In this section, the relative permittivity of the dielectric is set to  $\epsilon_r = 4.0$ , in order to reduce the phase velocity of the electromagnetic wave to beam velocity. Figure 10 shows the dispersion curves for a finitely thick annular beam with energy 660 keV and beam current 2.3 kA, in the absence of a magnetic field.

For an unmagnetized finitely thick annular electron beam, there are two kinds of surface space charge modes as in the annular plasma case at  $v = 0$ . One of them is due to the inner beam surface and denoted as “high-frequency space charge mode.” The other mode is attributed to the outer beam surface and denoted as “low-frequency space charge mode.” Both have fast and slow wave branches. In Figs. 10 and 11,  $F_{\text{HCh}}$  and  $S_{\text{HCh}}$  are the fast and slow high-frequency space charge modes, and  $F_{\text{LCh}}$  and  $S_{\text{LCh}}$  are the fast and slow low-frequency space charge modes, respectively.  $F_{\text{LCh}}$  and  $S_{\text{LCh}}$  exist near the lines  $\omega = k_z v + \omega_p/(\gamma\sqrt{2})$  and  $\omega = k_z v - \omega_p/(\gamma\sqrt{2})$ , respectively. The slow modes couple  $\text{TM}_{01}$  mode, resulting in the Cherenkov instability. The instability of  $S_{\text{LCh}}$  (Cherenkov instability 1) is much stronger than that of  $S_{\text{HCh}}$  (Cherenkov instability 2).

Similar to the plasma cases described in the previous section, the beam behaves like a moving charge layer for Cherenkov instability 1 in Fig. 10.  $F_{\text{LCh}}$  and  $S_{\text{LCh}}$  merge into a complex conjugate solution in strong interaction regions, similar to the solid beam case. On the other hand,

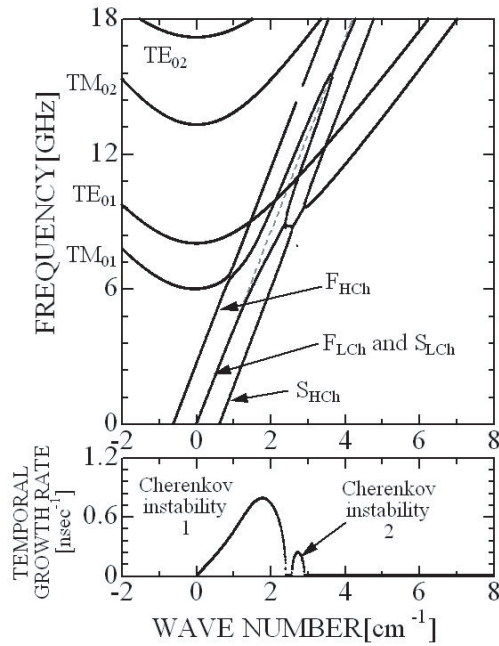


Fig. 10 Dispersion curves of a thin-walled annular beam in a dielectric-loaded waveguide with  $B_0 = 0$  T.

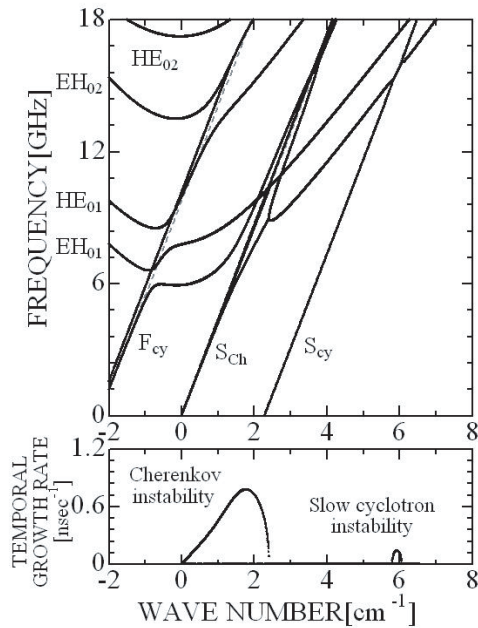


Fig. 11 Dispersion curves of a thin-walled annular beam in a dielectric-loaded waveguide with  $B_0 = 0.8$  T.

$F_{HCh}$  and  $S_{HCh}$  do not become complex conjugates. This might be caused by a double-layer-like behavior of the beam. As seen from Fig. 2, the axial electric fields are in the opposite direction on both the sides of the annulus. The Cherenkov interactions due to both the surface charges may compete with each other. Hence, overall the Cherenkov instability (Cherenkov instability 2) becomes weaker than Cherenkov instability 1.

Figure 11 shows the dispersion curves for a finitely thick annular electron beam with  $B_0 = 0.8$  T ( $\Omega > \omega_p$ ). In this case, there is little effect of the high-frequency space charge mode due to the inner wall. For such a magnetized electron beam, the predominant beam modes are the fast and slow space charge modes due to the volume perturbations, which form a complex conjugate mode  $S_{Ch}$  in the interaction region. Further, the fast ( $F_{cy}$ ) and slow ( $S_{cy}$ ) cyclotron modes exist near the lines  $\omega = k_z v + \Omega/\gamma$  and  $\omega = k_z v - \Omega/\gamma$ , respectively. The slow space charge and cyclotron modes couple with both the  $EH_{01}$  and  $HE_{01}$  modes, resulting in the Cherenkov and slow cyclotron instabilities. Instabilities for the  $EH_{01}$  mode are superior to those for the  $HE_{01}$  mode.

## 5. Discussion and Conclusion

Up to now, the thickness of the annulus is maintained at a constant value of  $\Delta_p = 0.1$  cm, as mentioned in Sec. 2. Here, we discuss numerically obtained results based on a solid beam, an infinitesimally thin annular beam, and a finitely thick annular beam. In Fig. 12,  $\Delta_p$  is varied, and the dependence of the temporal growth rate on  $\Delta_p$  is examined. The beam outer radius is fixed at 0.8 cm, and beam inner radius is varied with a fixed line charge density, i.e., keeping  $\omega_p \Delta_p$  constant. In the limit that the beam inner radius is zero, the growth rate of the Cherenkov and slow cyclotron instabilities of the finitely thick annular beam approaches the growth rate of the solid beam,  $\blacktriangle$  in Fig. 12.

The growth rate of the Cherenkov instability increases with decreasing  $\Delta_p$ . The growth rate of the slow cyclotron instability also increases with decreasing beam thickness and decreases near  $\Delta_p = 0$ . In the extreme case of  $\Delta_p \rightarrow 0$ , the corresponding beam is an infinitesimally thin annular beam. However, in the theoretical model, the finitely thick and infinitesimally thin annuli have different structures: the former has an internal structure between the inner and outer surfaces, and the latter is just a sheet without any internal structure.

Based on an infinitesimally thin annular beam, the Cherenkov and slow cyclotron instabilities can be analyzed following the new field theory considering the moving surface modulation. The growth rates obtained by the infinitesimally thin annular beam model are depicted by  $\bullet$  in Fig. 12.

For the a finitely thick annular beam in the present work,  $\omega_p \rightarrow \infty$  and  $\omega_h \rightarrow \infty$  when  $\Delta_p \rightarrow 0$  with a fixed  $\omega_p \Delta_p$ . As mentioned in Sec. 3, the cyclotron modes stay close to the line  $\omega = \omega_h$ , and plasma modes exist near the line  $\omega = 0$  in the plasma case. Hence, the cyclotron modes are affected by the fact that  $\omega_h \rightarrow \infty$ . Further, the Doppler shifted cyclotron modes of the beam are near the line of  $\omega = k_z v \pm \omega_h/\gamma$ , not the line of  $\omega = k_z v \pm \Omega/\gamma$ . On the other hand, in the infinitesimally thin model, the divergence of  $\omega_p$  is removed using the finite  $\omega_p \Delta_p$  in the limit of  $\omega_p \rightarrow \infty$  and  $\Delta_p \rightarrow 0$ . The slow cyclotron interaction

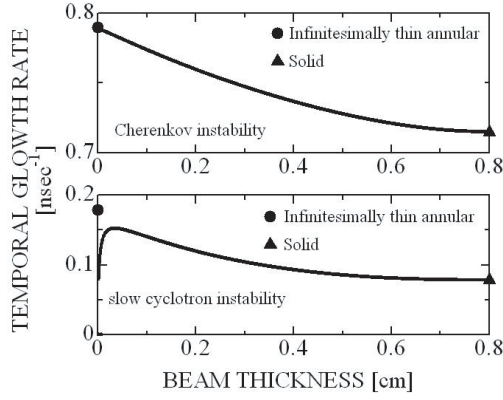


Fig. 12 The dependence of the temporal growth rate on the beam thickness.

occurs near the crossing point between  $\omega = k_z v - \Omega/\gamma$  and the waveguide mode. This difference causes a disagreement between the finitely thick and infinitesimally thin annular models for slow cyclotron instabilities in the limit of  $\Delta_p \rightarrow 0$ . For the Cherenkov interaction, such disagreement does not occur. Since the plasma modes are pushed down closer to the line  $\omega = 0$ , the Doppler shifted space charge modes of the beam are close to the line  $\omega = k_z v$  even when  $\omega_p \rightarrow \infty$ . The Cherenkov interaction is not affected much by the divergence of  $\omega_p$  attributed to the finitely thick annular model.

In conclusion, we developed a numerical code for a cylindrical waveguide with a finitely thick annular beam considering three-dimensional beam perturbations. The transverse perturbations of electrons appear as the surface electric charge at the fixed boundary and become important, especially for a weak guiding magnetic field ( $\omega_p > \Omega$ ). The surface wave modes exist in addition to the volume wave mode. A solid beam has only one surface, while a finitely thick annular beam has another surface inside the beam. The dispersion curves show two surface waves due to the two surfaces: high- and low-frequency surface wave modes. A solid plasma has only one surface wave mode due to the outer surface space charge. For a relatively strong magnetic field ( $\Omega > \omega_p$ ), surface modes become insignificant. A finitely thick annular beam drives the slow cyclotron and Cherenkov instability. The Cherenkov and slow cyclotron instabilities increase with decreasing  $\Delta_p$ , for a fixed  $\omega_p \Delta_p$ . In the limit of  $\Delta_p \rightarrow 0$ ,  $\omega_p$  and  $\omega_h$  diverge in the finitely thick model. The divergence affects the slow cyclotron instability. However,  $\Delta_p$  and  $\omega_p$  are finite in real devices. Hence, the finitely thick annular model is more realistic and important compared with the other beam models.

## Acknowledgments

This work was partially supported by a Grant-in-Aid for Scientific Research from the Ministry of Education, Science, Sports and Culture of Japan, and partially

performed under the Collaborative Research Program between NIFS and University of Tsukuba in cooperation with Japanese universities.

## Appendix: Dispersion Equation of a Finitely Thick Annular Beam

We consider the dielectric SWS system depicted in Fig. 1. Suitable functions for the cylindrical system are the Bessel functions, i.e.,  $J_m$  and  $N_m$ . In the inner vacuum region of the annular column,  $r < R_a - \Delta_p/2$ , the axial components of the electric and magnetic waves are

$$E_{1z}^{\text{va}} = A_+ J_m(k_\perp r) \quad \text{and} \quad B_{1z}^{\text{va}} = \frac{i}{c} A_- J_m(k_\perp r). \quad (\text{A. 1})$$

Here,  $k_\perp$  is the vertical wave number in vacuum,

$$k_\perp^2 = \frac{\omega^2}{c^2} - k_z^2. \quad (\text{A. 2})$$

In the beam column region,  $R_a - \Delta_p/2 < r < R_a + \Delta_p/2$ , the vertical wave number  $k_\pm$  is derived in Ref. [3] and given by

$$k_\pm^2 = \frac{-a_2 \pm \sqrt{a_2^2 - 4a_4 a_0}}{2a_4}. \quad (\text{A. 3})$$

Here,

$$\begin{aligned} a_4 &= \omega'^2 - \frac{\omega_p^2}{\gamma^3}, \\ a_2 &= - \left[ \left( \frac{\omega^2}{c^2} - k_z^2 \right) \left( \omega'^2 - \frac{\omega_p^2}{\gamma^3} \right) - \frac{\omega_p^2}{\gamma c^2} \left( \omega'^2 - \frac{\omega_p^2}{\gamma^3} \right) \right] \\ &\quad - \left[ \left( \frac{\omega^2}{c^2} - k_z^2 \right) \omega'^2 - \frac{\omega_p^2}{\gamma c^2} \omega'^2 \right] \left( 1 - \frac{\omega_p^2}{\gamma^3 \omega'^2} \right), \\ a_0 &= \Delta \omega'^2 \left( 1 - \frac{\omega_p^2}{\gamma^3 \omega'^2} \right), \\ \Delta &= \left( \frac{\omega^2}{c^2} - k_z^2 - \frac{\omega_p^2}{\gamma c^2} \frac{\omega'^2}{\omega'^2} \right)^2 - \left( \frac{\omega_p^2}{\gamma c^2} \frac{\omega'}{\omega'^2} \frac{\Omega}{\gamma} \right)^2, \end{aligned} \quad (\text{A. 4})$$

and

$$\begin{aligned} \omega' &= \omega - k_z v, \\ \omega'^2 &= (\omega - k_z v)^2 - (\Omega/\gamma)^2. \end{aligned} \quad (\text{A. 5})$$

Independent modes of the magnetized beam are those with  $k_+$  and  $k_-$  corresponding to the + and - signs in Eq. (A. 3), respectively. The axial components are given by

$$\begin{aligned} E_{1z}^{\text{b}} &= D_m^+ J_m(k_+ r) + E_m^+ N_m(k_+ r) \\ &\quad + D_m^- J_m(k_- r) + E_m^- N_m(k_- r), \\ B_{1z}^{\text{b}} &= \frac{i}{c} [F_m^+ J_m(k_+ r) + G_m^+ N_m(k_+ r)] \\ &\quad + \frac{i}{c} [F_m^- J_m(k_- r) + G_m^- N_m(k_- r)]. \end{aligned} \quad (\text{A. 6})$$

In the outer vacuum region of the annular column,  $R_a + \Delta_p/2 < r < R_d$ , the axial components become

$$\begin{aligned} E_{1z}^{\text{va}} &= D_m^{\text{va}} J_m(k_\perp r) + E_m^{\text{va}} N_m(k_\perp r), \\ B_{1z}^{\text{va}} &= \frac{i}{c} [F_m^{\text{va}} J_m(k_\perp r) + G_m^{\text{va}} N_m(k_\perp r)], \end{aligned} \quad (\text{A. 7})$$

and in the dielectric region,  $R_d < r < R_w$ ,

$$\begin{aligned} E_{1z}^{\text{d}} &= D_m^{\text{d}} J_m(x_\perp r) + E_m^{\text{d}} N_m(x_\perp r), \\ B_{1z}^{\text{d}} &= \frac{i}{c} [F_m^{\text{d}} J_m(x_\perp r) + G_m^{\text{d}} N_m(x_\perp r)]. \end{aligned} \quad (\text{A. 8})$$

Here,  $x_\perp$  is the vertical wave number in the dielectric with the dielectric constant  $\epsilon_r$ .

$$x_\perp^2 = \epsilon_r \frac{\omega^2}{c^2} - k_z^2. \quad (\text{A. 9})$$

Transverse field components can be derived from the axial components in all regions.

For a bounded system, Maxwell's equations should be solved subject to the appropriate boundary conditions. At the beam surface ( $r = R_a + \Delta_p/2$  or  $r = R_a - \Delta_p/2$ ), the following four independent equations are obtained in accordance with the methods presented in Refs. [3, 4].

$$E_{1z}^{\text{b}} = E_{1z}^{\text{va}}, \quad (\text{A. 10})$$

$$E_{1\theta}^{\text{b}} = E_{1\theta}^{\text{in}}, \quad (\text{A. 11})$$

$$B_{1z}^{\text{b}} = B_{1z}^{\text{va}}, \quad (\text{A. 12})$$

$$E_{1r}^{\text{b}} + \frac{\sigma_1}{\epsilon_0} = E_{1r}^{\text{va}}. \quad (\text{A. 13})$$

Here,  $\sigma_1$  is the surface charge density at the beam surface. Superscripts "va" and "b" indicate the vacuum and beam sides on the surface, respectively.

At the outer boundary  $r = R_a + \Delta_p/2 (= R2)$ , the four equations (A. 10)-(A. 13) correlate beam fields of (A. 6) with vacuum fields of (A. 7). Representing field components by  $D_m^+$ ,  $E_m^+$ ,  $D_m^-$ , and  $E_m^-$  in the beam and  $D_m^{\text{va}}$ ,  $E_m^{\text{va}}$ ,  $F_m^{\text{va}}$ , and  $G_m^{\text{va}}$  in the vacuum region, the four equations are expressed as the following formula.

$$[MC]_{R2} \cdot \begin{bmatrix} D_m^{\text{va}} \\ E_m^{\text{va}} \\ F_m^{\text{va}} \\ G_m^{\text{va}} \end{bmatrix} = [MA]_{R2} \cdot \begin{bmatrix} D_m^+ \\ E_m^+ \\ D_m^- \\ E_m^- \end{bmatrix}. \quad (\text{A. 14})$$

Here,  $[MA]_{R2}$  and  $[MC]_{R2}$  are the  $4 \times 4$  matrix composed of the coefficients of  $(D_m^+, E_m^+, D_m^-, E_m^-)$  and  $(D_m^{\text{va}}, E_m^{\text{va}}, F_m^{\text{va}}, G_m^{\text{va}})$ , respectively. Similarly, at the inner boundary  $r = R_a - \Delta_p/2 (= R1)$

$$[MA]_{R1} \cdot \begin{bmatrix} D_m^+ \\ E_m^+ \\ D_m^- \\ E_m^- \end{bmatrix} = [MC]_{R1} \cdot \begin{bmatrix} A_+ \\ A_- \end{bmatrix}. \quad (\text{A. 15})$$

Here,  $[MA]_{R1}$  is the  $4 \times 4$  matrix composed of the coefficients of  $(D_m^+, E_m^+, D_m^-, E_m^-)$ , and  $[MC]_{R1}$  is the  $4 \times 2$  matrix composed of the coefficients of  $(A_+, A_-)$ .

From eqs. (A. 14) and (A. 15), we can derive the relationship between  $(D_m^{\text{va}}, E_m^{\text{va}}, F_m^{\text{va}}, G_m^{\text{va}})$  and  $(A_+, A_-)$ .

$$\begin{aligned} \begin{bmatrix} D_m^{\text{va}} \\ E_m^{\text{va}} \\ F_m^{\text{va}} \\ G_m^{\text{va}} \end{bmatrix} &= [MC]_{R2}^{-1} \cdot [MA]_{R2} \cdot [MA]_{R1}^{-1} \cdot [MC]_{R1} \cdot \begin{bmatrix} A_+ \\ A_- \end{bmatrix} \\ &= [X] \cdot \begin{bmatrix} A_+ \\ A_- \end{bmatrix}. \end{aligned} \quad (\text{A. 16})$$

Here,  $[X] = [MC]_{R2}^{-1} \cdot [MA]_{R2} \cdot [MA]_{R1}^{-1} \cdot [MC]_{R1}$ . Similarly, for the dielectric-vacuum boundary at  $r = R_d$ , we express the condition using the  $4 \times 4$  matrix  $[MD]$ .

$$[MD]_{Rd} \cdot \begin{bmatrix} D_m^{\text{d}} \\ E_m^{\text{d}} \\ F_m^{\text{d}} \\ G_m^{\text{d}} \end{bmatrix} = [MC]_{Rd} \cdot \begin{bmatrix} D_m^{\text{va}} \\ E_m^{\text{va}} \\ F_m^{\text{va}} \\ G_m^{\text{va}} \end{bmatrix}. \quad (\text{A. 17})$$

Finally, using (A. 16) and (A. 17), we can derive the relationship between  $(D_m^{\text{d}}, E_m^{\text{d}}, F_m^{\text{d}}, G_m^{\text{d}})$  and  $(A_+, A_-)$  as

$$\begin{aligned} \begin{bmatrix} D_m^{\text{d}} \\ E_m^{\text{d}} \\ F_m^{\text{d}} \\ G_m^{\text{d}} \end{bmatrix} &= [MD]_{Rd}^{-1} \cdot [MC]_{Rd} \cdot [X] \cdot \begin{bmatrix} A_+ \\ A_- \end{bmatrix} \\ &= [Y] \cdot \begin{bmatrix} A_+ \\ A_- \end{bmatrix}. \end{aligned} \quad (\text{A. 18})$$

Here,  $[Y] = [MD]_{Rd}^{-1} \cdot [MC]_{Rd} \cdot [X]$ . This equation correlates electromagnetic fields in the dielectric region with those in the vacuum region inside the beam.

At the wall of  $r = R_w$ , two electric field components tangential to the wall,  $E_{1z}$  and  $E_{1\theta}$ , should be zero.

$$E_{1z}^{\text{d}}|_{Rw} = D_m^{\text{d}} J_m(x_\perp R_w) + E_m^{\text{d}} N_m(x_\perp R_w) = 0. \quad (\text{A. 19})$$

$$E_{1\theta}^{\text{d}} = \frac{\omega/c}{x} [F_m^{\text{d}} J'_m(x_\perp r) + E_m^{\text{d}} N'_m(x_\perp r)] = 0. \quad (\text{A. 20})$$

Expressing  $D_m^{\text{d}}$ ,  $E_m^{\text{d}}$ ,  $F_m^{\text{d}}$ , and  $G_m^{\text{d}}$  by  $A_+$  and  $A_-$  using (A. 18), eqs. (A. 19) and (A. 20) take the following form:

$$\begin{bmatrix} p_{z+} & p_{z-} \\ p_{\theta+} & p_{\theta-} \end{bmatrix} \cdot \begin{bmatrix} A_+ \\ A_- \end{bmatrix} = 0. \quad (\text{A. 21})$$

Then, the dispersion equation given by

$$p_{z+} \cdot p_{z-} - p_{\theta+} \cdot p_{\theta-} = 0. \quad (\text{A. 22})$$

- [1] A.S. Gilmour, Jr., *Principles of Traveling Wave Tubes* (Artech House, Boston, 1994) P.233.
- [2] R.J. Barker and E. Schamiloglu eds, *High-Power Microwave Sources and Technologies* (IEEE Press, New York, 2001) P.284.
- [3] O. Watanabe *et al.*, Phys. Rev. E. **63**, 056503 (2001).
- [4] K. Ogura *et al.*, Jpn. J. Appl. Phys. **42**, 7095 (2003).
- [5] J.R. Pierce, *Traveling-Wave Tube* (Van Nostrand, Toronto, 1950) P.168.
- [6] K. Ogura *et al.*, J. Plasma Phys. **72**, 905 (2006).
- [7] H. Yamazaki *et al.*, IEEJ Trans. FM **125**, 739 (2005).
- [8] Y. Kiuchi *et al.*, Trans. Fusion Sci. Technol. **51**, 331 (2007).